This is a preprint, the final version is subject to change, of the American Mineralogist (MSA)
Cite as Authors (Year) Title. American Mineralogist, in press.
(DOI will not work until issue is live.) DOI: http://dx.doi.org/10.2138/am.2014.4626

REVISE2

04-12-2013

The cooling kinetics of plagioclase revealed by electron microprobe mapping

Gianluca Iezzi[1,2*], Silvio Mollo[2], Edisa Shaini[1], Andrea Cavallo[2], Piergiorgio Scarlato[2]

[1]Dipartimento INGEO, Università G. d'Annunzio, Via Dei Vestini 30, I-66013 Chieti, Italy
[2]Istituto Nazionale di Geofisica e Vulcanologia. Via di Vigna Murata 605 00143 Roma, Italy

[*]Corresponding author: phone: +39 0871 3556147, Fax: +39 0871 3556047,
email: g.iezzi@unich.it

ABSTRACT

In this study we have used electron microprobe mapping to investigate plagioclase compositional evolution due to cooling kinetics. We re-analyzed five run-products from a prior study (Iezzi et al. 2011), crystallized by cooling a natural andesitic melt from 1300 to 800 °C at 25, 12.5, 3, 0.5 and 0.125 °C/min under atmospheric pressure and air redox state. As the cooling rate decreases, the texture of large plagioclases changes from skeletal to hollow to nearly equant. In this study, we use x-ray map data to obtain a database of 12275 quantitative chemical analyses. The frequency of An-rich plagioclases showing disequilibrium compositions substantially increases with increasing cooling rate. At 25 and 12.5 °C/min the distribution is single-mode and narrow, at 0.5 and 0.125 °C/min is single-mode but very broad, whereas at the intermediate cooling rate of 3 °C/min two distinct plagioclase populations are present. This intermediate cooling rate is fast enough to cause departure from equilibrium for the crystallization of the An-rich population but also sufficiently slow that An-poor plagioclases nucleate from the residual melt. We interpret our findings in the context of time-temperature-transformation (TTT) diagrams, and infer the crystallization kinetics of plagioclase in the experiments. Compositional trends and our inferences regarding TTT systematics are consistent with two discrete nucleation events that produced separate populations of plagioclase (i.e., An-rich and An-poor populations) at 3 °C/min. Using plagioclase-melt pairs as input data for the thermometric reaction between An and Ab components, we find that plagioclase mirrors very high (near-liquidus) crystallization temperatures with increasing cooling rate. These results have important implications for the estimate of post-eruptive solidification conditions. Lava flows and intrusive bodies from centimeters to a few meters thick are characterized by a short solidification time and a significant thermal diffusion. Under such circumstances, it is possible to crystallize plagioclases with variable and disequilibrium chemical compositions simply by cooling a homogeneous andesitic melt. X-ray element maps enrich the study of plagioclase compositional variations generated under conditions of rapid cooling.

Keywords: andesite, plagioclase, EPMA map, cooling, crystallization, thermometer

Running title: microprobe mapping of plagioclase

INTRODUCTION

Plagioclase is the most common mineral in igneous rocks. Over other crystal phases, plagioclase has important advantages in preserving records of the chemical and physical evolution of magmas due to the slow coupled CaAl-NaSi interdiffusion that inhibits the re-equilibration of growing crystals and favors the retention of original element concentrations (Grove et al. 1984; Morse 1984; Liu and Yund 1992; Baschek and Johannes 1995). This ensures that plagioclase chemical and textural zoning can be used for deciphering magmatic events (cf. Putirka 2008) as it is also highlighted by the rare occurrence of compositionally homogeneous plagioclases in nature (Smith and Brown 1988; Liu and Yund 1992; Baschek and Johannes 1995; Deer et al. 2007). Indeed, disequilibrium textures and compositions of plagioclase are frequently studied under natural and laboratory conditions (Hammer 2006, Iezzi et al. 2008, 2011; Brugger and Hammer 2010; Del Gaudio et al. 2010; Mollo et al. 2011a; 2011b; 2012a; 2012b; Lanzafame et al. 2013).

Cooling, crystal settling, convection and mixing in magma chambers allow crystallization of plagioclase phenocrysts with compositions that deviates from equilibrium (Marsh 1988; Singer et al. 1995; Couch et al. 2001; Pietranik et al. 2006). Disequilibrium crystals (microphenocrysts) can also solidify when magmas rise to the surface in response to rapid volatile degassing imposed by decompression paths (Couch et al. 2003; Blundy et al. 2006; Brugger and Hammer 2010; Frey and Lange 2011). In addition, rapidly cooled plagioclases are observed at the margin of small intrusions and the outermost portion of lavas (Ujike 1982; Loomis and Welber 1982; Chistyakova and Latypov 2009; Del Gaudio et al. 2010; Mollo et al. 2012a; 2011b). This latter process has been experimentally investigated for basic magmas (Hammer 2006; Mollo et al. 2011a), but is still poorly unconstrained for andesitic melts where plagioclase is by far the most abundant mineral. Since the cooling rate may dictate the compositional evolution of plagioclase in andesitic lavas (Tamura et al. 2003; Mattioli et al. 2006), it is important to quantify this process for discriminating between pre- and post-eruption solidification conditions.

Recently, Iezzi et al. (2011) experimentally investigated the variation of plagioclase textures in an andesitic melt as a function of cooling rate. In this study, we focus on the compositional variation of these plagioclases keeping in mind that crystallization kinetics are generally studied through analytical data collected by selection of single point analyses and/or crystal core-to-rim analytical profiles (e.g., Singer et al. 1995; Hammer 2008; Mollo et al. 2011a; Brugger and Hammer 2010; Iezzi et al. 2011). Conversely, we have performed X-ray electron microprobe mapping on relative large areas to guarantee the analysis of the whole spectrum of compositions characterizing tiny and large crystals (Pownceby and McRae 2007a, 2007b; Prêt et al. 2010a, 2010b; Pieczka et al.

2011; Muir et al. 2012; Shea and Hammer, 2013). Although microprobe mapping is time-consuming, a lack of spatial information on the distribution of key element concentrations prompted us to re-analyze the five run-products synthesized by cooling a natural andesitic melt from 1300 to 800 °C at 25, 12.5, 3, 0.5 and 0.125 °C/min under atmospheric pressure and air redox state by Iezzi et al. (2011).

The obtained broad database of plagioclase chemical analyses allows to construct distribution histograms and frequency curves of An-rich disequilibrium plagioclases. In addition, plagioclase-melt pairs as input data for the thermometric reaction between An and Ab components (Putirka 2008) allow to model the effect of cooling rate on the prediction of crystallization temperatures; this has important implications for the estimate of the thermal path of rapidly cooled lava flows and dikes. The experimental conditions considered here are relevant for dry, aphyric and superheated andesitic lavas produced during the eruption of degassed and crystal-free magmas (Tamura et al. 2003; Mattioli et al. 2006; Vetere et al. 2013), and for a few meter-thick dikes intruded in cold wall-rocks. Cooling rates of 25, 12.5 and 3 °C/min are pertinent for the outermost (a few centimeter- and decimeter-thick) parts of lavas, whereas cooling rates of 0.5 and 0.125 °C/min operates in the innermost portions (Dunbar et al. 1995; Neri 1998; Xu and Zhang 2002; Burkhard 2005; Harris et al. 2005).

STARTING MATERIAL AND METHODS

The starting material discussed in this study is a calc-alkaline glassy andesitic scoria from Panarea Island (Aeolian Islands, Italy) previously studied by Dolfi et al. (2007). The rock was finely ground and ~10 g of powder was loaded in a Pt-crucible and melted two times in air at 1400 °C for 200 min. The obtained starting material did not contain any crystalline phase (see Iezzi et al. 2011 for further details). A Deltech DT-31 vertical rapid-quench furnace was used to prepare the starting glass and to perform the cooling rate experiments. At the beginning of cooling, the starting glassy material was held at 1400 °C for 40 min, i.e., 234 °C above the melt liquidus temperature of 1166 °C (see Iezzi et al. 2011 for further details). Successively, the temperature was lowered to 1300 °C in 5 min. Below 1300 °C, five different cooling rates of 25, 12.5, 3, 0.5 and 0.125 °C/min were applied and the final quenching temperature was 800 °C. A further experiment was run at 1400 °C (dwell time of 40 min), cooled in 5 min to 1300 °C, and then quenched. The analysis of this run-product did not reveal crystals and its chemistry was considered the starting melt composition reported here: SiO_2 = 58.52 (±0.7), TiO_2 = 0.59 (±0.06), Al_2O_3 = 17.24 (±0.49), Fe_2O_3 = 7.67 (±0.35), MnO = 0.18

(±0.04), MgO = 4.14 (±0.17), CaO = 7.73 (±0.33), Na_2O =2.46 (±0.07), K_2O = 1.97 (±0.01), P_2O_5=0.15(±0.02), all in wt.%.

The five run-products were re-analyzed with an electron probe micro-analyzer (EPMA) JEOL-JXA8200 combining EDS-WDS (five spectrometers with twelve crystals) installed at Istituto Nazionale di Geofisica e Vulcanologia, Roma (Italy). Analyses were performed using accelerating voltage of 15 kV, electric current of 10 nA and beam size of 1 μm^2. X-ray EPMA-WDS chemical maps were performed by stage rastering, keeping the electron beam stationary while stage moves. The collected EPMA point analyses were acquired with constant distances in each run-product as reported in Table 1; hence, each pixel on the images of Fig. 1 corresponds to a resolution of 2 μm for run-products cooled at 25, 12.5 and 3 °C/min and 4 μm for those at 0.5 and 0.125 °C/min (Table 1). Each point analysis measured the quantities of Al, Na, Si, Ca and K by using the following crystals: TAP for Na and Al and PET for Si, Ca and K. These five elements were then converted in oxides using classical analytical EPMA protocols.

The microprobe maps sampled representative areas for each run-product (Table 1). These areas were selected on the basis of previous textural observations by Iezzi et al. (2011) that underlined as both the crystal amount and the maximum size dimension of plagioclase decrease with increasing cooling rate. Considering that microprobe maps are time-consuming (Pownceby et al. 2007a; Pret et al. 2010a), we were forced to use a rapid counting time of 120-20 ms on peak and background, respectively, for each point analysis (as aforementioned the distance between analytical point is 2 and 4 μm, Table 1). The area of maps ranged between 1 and 5 mm^2 with resolution of 310×242 to 1024×1024 $pixel^2$. A linear off-peak correction was used due to the high abundance of the chosen elements as major constituents of plagioclase. By correcting the intensity of each point analysis for background, k factors and matrix effects, digital compositional images in Fig. 1 provide a complete quantitative analysis for each pixel scanned. The software provided by JEOL Ltd. allowed to export point analyses for each map on the basis of x-y coordinates. To check the reliability of exported data, we also analyzed ten single crystals for each run-product using longer counting times of 20 s on peak and 10 s on background, respectively. Differences between these two analytical methods are lesser than 1 % for SiO_2, Al_2O_3 and CaO, 1.5 % for Na_2O and 5 % for K_2O; thereby, each point analysis, i.e. pixel, into an EPMA map is a quantitative determination of these five major oxide components (Fig. 1).

A substantial data screening has been performed on the whole data acquired. We considered to be a quantitative chemical composition of plagioclase only the EPMA point analyses with 43.2< SiO_2 <68.7, 18.3< Al_2O_3 <36.7, 0< CaO <20.2, 0< Na_2O <11.8 and 0< K_2O <16.9 wt.% included in the ternary feldspar doagram (Deer et al. 1997), with the sum of these five oxide components

comprised between 99 and 101 wt.%. Mineral formula based on 8 oxygens show that: 0.96<Ca+Na+K<1.04 a.p.f.u. and 3.96<Si+Al<4.04 a.p.f.u.. The selection process yielded a dataset of 12275 analyses reported into the Microsoft Excel spreadsheet available online as supplementary material.

RESULTS

The compositional variations of plagioclase is displayed in Fig. 1, together with the anorthite molecular variations corresponding to calculated mol.% of $CaAl_2Si_2O_8$ (Fig. 1b). The textural variation of experimental run-products previously described by Iezzi et al. (2011) can be further constrained by chemical maps as follows: (i) plagioclases and Fe–Ti oxides are always present, whereas clinopyroxene appears at 0.5 and 0.125 °C/min; (ii) plagioclase is the most abundant phase and its content significantly increases with increasing cooling rate (Table 1); (iii) the crystallization of plagioclase (and Fe–Ti oxide) starts homogeneously; iv) larger plagioclases are invariably surrounded by smaller acicular and skeletal crystals depleted in Al_2O_3 (Fig. 1a) and An (Fig. 1b); (v) at 25, 12.5 and 3 °C/min, crystal-rich patches are dispersed into the matrix glass where larger plagioclases grown with skeletal, hollow and irregular shapes (Fig. 1); vi) at 0.5 and 0.125 °C/min, larger plagioclases, interconnected by a continuous network of crystals, have a near-regular, equant and tabular shapes (Fig. 1). The crystallographic direction of preferential growth of acicular plagioclases should be 100 (Iezzi et al. 2011). The textural features of our plagioclases are very similar to those reported in Lofgren (1974) and (1980) and Corrigan (1982) grown from basaltic melts, as well as those recently reported in Shea and Hammer (2013) solidified either by cooling and decompression from an hydrous basaltic-andesite melt with a SiO_2 content of 55.65 wt.%.

The plagioclase compositional variation is also presented in Fig. 2. As the cooling rate is increased, plagioclases are progressively enriched in Al_2O_3 and CaO, and depleted in SiO_2, Na_2O and K_2O (Fig. 2). This chemical variation parallels the less differentiated composition of the residual melt. Due to lower degrees of crystallization with increasing cooling rate (Table 1), residual melts progressively change from dacite to andesite approaching to the bulk rock starting composition (see data reported into the Microsoft Excel spreadsheet available online as supplementary material).

DISCUSSION

Statistical distributions of plagioclase composition and their possible crystallization mechanism

Frequency curves and histograms calculated using 20 bins for each 5 mol.% of An in plagioclase are plotted in Fig. 3 together with the An content of the residual melt (^{melt}An) that increases from 34 to 50 mol.% with increasing crystal content (Table 1). The distribution analysis highlights that the number, shape and position of An-frequency peaks change as a function of cooling rate (Fig. 3). We observe that: (i) at 25 °C/min, one single almost symmetric and narrow peak is found at An_{87}; (ii) at 12.5 °C/min, the peak is still at An_{87} but the distribution is moderately asymmetric with a left-shoulder; (iii) at 3 °C/min, a bimodal distribution occurs with two peaks at An_{92} and An_{52}, and; (iv) at both 0.5 and 0.125 °C/min, single-mode distributions are found over a number of compositional classes markedly larger than those measured under faster cooling rates. The dashed line displayed in Fig. 3 is the composition (i.e., An_{57}) of plagioclase in equilibrium with the andesitic melt at 800 °C (see Iezzi et al., 2011 for further details). As the degree of cooling is increased, the peak of An-frequency curves shifts towards values higher than the equilibrium composition (Fig. 3). Notably, at 3 °C/min, the An_{52} peak is close to the equilibrium value of An_{57}; in contrast, the An_{92} peak is close to the maximum disequilibrium composition of An_{97} (Fig. 3). Such a compositional variation reflects two crystallization events: at the early stage of cooling, An-rich plagioclases readily crystallized from the starting andesitic liquid; later, relatively An-poor crystals formed from the more differentiated melt. At the early-stage the plagioclase crystallization is mostly dictated by the homogenous nucleation of isolated An_{97} microlites (Fig. 1b; Fig. 3). At 25 °C/min and 12.5 °C/min, An-rich microlites start to agglomerate forming relative large and texturally immature An-rich plagioclases (Fig. 1b).

As the cooling rate decreases to 0.125 °C/min, the early nucleation of An-rich crystals is followed by several multiple "agglomeration" events. We term this type of crystallization agglomeration or coalescence according to *in-situ* crystallization observations by Schiavi et al. (2009); differently from "coarsening" (Zhang 2008; Higgins 2011), crystal agglomeration does not imply a dissolution of smaller crystals and the simultaneous growth of larger ones. The plagioclases re-investigated in this study were interpreted to grow by agglomeration, mainly on the basis of their crystal size distribution (CSD) evolution (Iezzi et al. 2011); as the cooling rate decreases from 25 to 0.125 °C/min, the CSD of plagioclase progressively rotates counterclockwise and changes from near straight lines to curves; this CSD evolution has been interpreted by Iezzi et al. (2011) as an increment of the crystal agglomeration rate as the cooling rate decreases.

The crystallization mechanism, inferred *via* CSD data by Iezzi et al. (2011), appears to be corroborated by the nearly absence of zoned plagioclases (Fig. 1b). If the growth of these large plagioclases was accomplished only by a continuous feeding of chemical species from the surrounding melt, they should exhibit a certain degree of crystal zonation from Al- and Ca-rich cores

238 to Na- and Si-rich rims, in agreement with the imposed experimental decrement of temperature. This
239 is not the case as indicated by each run-product (Fig. 1a and 1b).

240 We suggest that the mechanism of attachment could be similar to that observed at a relative
241 low amount of crystal content by Schiavi et al. (2009) and possibly explained by the emerging
242 theory of aggregation by self-orientation of sub-micrometric early-formed primary crystals (Teng
243 2013 and references therein). However, TEM investigations are required to elucidate in full if this
244 aggregation-based model is applicable to crystals growing from silicate melts; secondary single
245 crystals grown by orientation aggregation of tiny primary crystals can be only revealed *ex-situ* by the
246 presence of peculiar microsturctures at a sub-micrometric scale (Teng 2013). An alternative
247 explanation for the crystallization of plagioclases displayed in Fig. 1 could also be a dendritic
248 growth followed by ripening; Welsch et al. (2013) inferred that in olivines the occurrence of narrow
249 strips strongly enriched in slow diffusing cations (i.e P, Al and Cr) testifies to a dendritic growth; in
250 the case of our plagioclases, dendritic crystallization followed by a ripening around early-formed
251 branches should be revealed by thin lines strongly depleted (for early-formed An-rich dendrites) or
252 enriched (for the melt surrounding An-rich dendrites) in Si. Although this can not be completely
253 discarded by SiO_2 chemical maps (Fig. 1a), since possible early-formed dendrites could be only few
254 μm in thickness and thus below the resolution of X-ray maps, we prefer the interpretation of crystal
255 aggregation being the larger plagioclases frequently characterised by the occurrence of small An-rich
256 and-poor areas (Fig. 1b).
257
258 **Metastable nucleation of plagioclase**
259 There is general consensus that Al-rich crystal phases, i.e., plagioclase, clinopyroxene and
260 spinel, are more favored to nucleate under dynamic conditions as demonstrated by laboratory studies
261 (Kirkpatrick 1983; Hammer 2006, 2008; Iezzi et al. 2008, 2011; Brugger and Hammer 2010; Del
262 Gaudio et al. 2010; Mollo et al. 2010, 2011a, 2011b) and chemical data from naturally cooled
263 magmas (Loomis 1981; Ujike 1982; Pietranik et al. 2006; Chistyakova and Latypov 2009; Mollo et
264 al. 2011b). In the case of plagioclase, the kinetically-controlled exchange reaction between
265 Al+Ca+Fe+Mg and Si+Na+K (Fig. 2) is mainly controlled by the increasing compatibility of Al
266 with respect to Si in rapidly growing crystals (Mollo et al. 2011a and references therein). According
267 to the nucleation theory, metastable phases that form in dynamic conditions apparently must
268 overstep a lower energetic barrier than do the thermodynamically stable phases (Kirkpatrick 1983;
269 Lasaga 1997; Zhang 2008; Iezzi et al. 2008, 2009 and 2011).
270 Below the liquidus temperature, nucleation requires random compositional fluctuations of
271 molecular units in the melt and stable nuclei can form only when the local arrangement of these units

attains a critical dimension (Roskoz et al. 2006a, 2006b; Zhang 2008). Since compositional fluctuations in the melt imply the rearrangement (breaking and formation) of chemical bonds, probabilistic fluctuations of molecular units with strong chemical bonds (i.e., network-forming cations) are less abundant and can explore a limited compositional space, i.e., the compositional difference between the initial liquid and the final structural arrangement (Roskosz et al. 2006a, 2006b). The opposite occurs for chemical elements that rapidly diffuse in the melt (i.e., network-modifiers cations). The energetic barrier of nucleation roughly scales with the number of ^{IV}Si-O bonds and to a less extent of ^{IV}Al-O bonds, i.e., the degree of polymerization and the average bond strength (Kirkpatrick 1983; Dingwell 2006; Iezzi et al. 2008, 2009, 2011).

Using major oxide analyses of crystal and liquid, we have calculated the difference ($^{plg\text{-}melt}\Delta$) between the chemistry of plagioclase and that of the andesitic bulk composition. Results reveal that $^{plg\text{-}melt}\Delta SiO_2$ decreases by 27 % with increasing cooling rate; in contrast, $^{plg\text{-}melt}\Delta Al_2O_3$ increases by 78 %. The systematic enrichment of Al_2O_3 in plagioclase (Fig. 2) parallels the higher mobility of Al in the melt relative to that of Si (Mysen and Richet 2005; Zhang 2008). This implies that, although the tetrahedral framework structure is the same, SiO_2-rich crystals are delayed with respect to SiO_2-poor ones under kinetically-controlled conditions (Kirkpatrick 1983; Iezzi et al. 2008).

Time-temperature-transformation (TTT) diagram

The structural re-equilibration of a silicate melt depends on the relaxation time τ that, in turn, results from the Maxwell relation, $\tau = \eta/G$, where η is the viscosity of the melt and G is the shear modulus. The latter yields a mean value of about 10 GPa (Dingwell 1995; Webb 2005). The macroscopic relaxation (i.e., viscosity) of a natural silicate melt mainly reflects the SiO_2 variation of the melt itself due to its longest time to re-equilibrate relative to that of other oxides (Webb 2005; Dingwell 2006). As recently demonstrated by Vetere et al (2013), the relaxation time is orders of magnitude lower than rapid cooling rates (10^1-10^2 °C/min) obtained in laboratory. At temperature of 1300 °C and time duration of 2 hours, the chemical diffusion is relatively rapid leading to a complete chemical homogenization of the melt before nucleation (Vetere et al. 2013). This implies that the crystallization path can be interpreted by means of time-temperature-transformation (TTT) diagrams (Uhlmann et al. 1979; Lasaga, 1997; Vetere et al. 2013), especially at the early stage of crystallization. Conversely, the crystallization of successive crystals is less interpretable by TTT diagrams due to the occurrence of heterogeneous substrata and the relative slow diffusion of chemical species around early formed crystals (Vetere et al. 2013).

According to the nucleation theory (Lasaga, 1997; Fokin et al. 2003; Zhang, 2008; Iezzi et al. 2009), some important parameters control the shape and size of the TTT diagram, i.e., the nucleation

306 temperature (T), the nucleation rate (I), the degree of undercooling (ΔT), and the incubation time (τ).
307 In particular, T_{max} is defined as to the temperature at which the nucleation rate is maximum (I_{max})
308 and the incubation time is minimum (τ_{min}). T_{max}, I_{max} and τ_{min} are controlled by the energetic
309 competition between thermodynamic and kinetic barriers (i.e., chemical diffusion) as well as by the
310 composition of the melt (Lasaga 1997; Fokin et al. 2003). It is worth stressing that TTT diagrams
311 have never attracted considerable attention in Earth Sciences and, due to the paucity of data, only
312 qualitative information can be retrieved by our experiments (Vetere et al. 2013). In particular, Fig. 4
313 shows a schematic reappraisal based on three different TTT diagrams ideally comprised between the
314 melting (or liquidus) temperature (T_m) of the andesitic bulk composition and the glass transition (T_g)
315 temperature. As the temperature decreases (or the degree of undercooling increases), the nucleation
316 rate first increases to a maximum value and then progressively decreases (Fig. 4); notably, this
317 behavior determines the classical asymmetric Gaussian shape of the TTT diagram, i.e. the so-called
318 "nose shape". Fig. 4 highlights that successive TTT curves (red, blue and green curves) show lower
319 values for T_m and I_{max}, whereas T_g and τ_{min} increase, i.e. the breadth in T of the nose shape decreases
320 (Lasaga 1997; Fokin et al. 2003; Iezzi et al., 2009; Vetere et al. 2013 and references therein). These
321 variations are due to the more differentiated composition of the residual melt (Fig. 3) as the degree
322 of crystallization increases (Table 1). We therefore assume that the TTT diagram in red represents
323 the andesite initial composition (Fig. 4), whereas TTT diagrams in blue and green indicate the
324 residual melts resulting after different nucleation events or pulses. As a function of the imposed
325 cooling rate, the crystal growth of plagioclases summarized in Fig. 4 virtually occurs in the time
326 comprised between two adjacent TTT curves (Vetere et al. 2013). The cooling rates of 25, 3 and
327 0.125 °C/min at which the plagioclase shows major compositional variations (Figs. 1, 2 and 3) are
328 also depicted in Fig. 4 using dashed lines.
329 According to Iezzi et al. (2011), the critical cooling rate of the andesitic melt is 37 °C/min
330 and each cooling rate above this value do not intercept the TTT diagram (in red), causing the
331 solidification of a glassy product (Fig. 4). At 25 °C/min, the TTT diagram (in red) is intercepted
332 below the value of I_{max} (Fig. 4). Consequently, the degree of crystallization is low (i.e., 10 vol.%;
333 Table 1) and the plagioclase shows minor compositional variations (i.e., An_{80-96}; Fig. 3) due to the
334 fast cooling kinetics. Although plagioclase crystals form under high degrees of undercooling (i.e.,
335 below T_{max}), their composition is drastically enriched in Al and depleted in Si accounting for the
336 kinetically-controlled cation re-distribution reaction (Mollo et al., 2011a).
337 At the intermediate cooling rate of 3 °C/min, two TTT curves are intercepted above and
338 below the value of I_{max}, respectively (Fig. 4). The first TTT line (in red) is intercepted at the early
339 stage of cooling favoring the nucleation of An_{90-96} plagioclases (Fig. 3). As the crystallization

proceeds, the melt becomes depleted in anorthite and its more evolved composition is represented by the second TTT diagram (in blue) depicted in Fig. 4. Plagioclase crystals from this melt have anorthite contents lower than those measured at the early stage of crystallization accounting for high temperature conditions (Fig. 4). This explains the bimodal compositional distribution showing two different peaks at An_{92} and An_{52}, respectively (Fig. 4).

At 0.125 °C/min, several TTT curves are intercepted and, therefore, the nucleation initiates at low degrees of undercooling, i.e. remarkably above T_{max} (Fig. 4). The number of nucleation events progressively increases as the cooling proceeds and the melt becomes more differentiated. As expected, plagioclases showing the lowest anorthite content (Fig. 3) crystallize only when the most differentiated melt is intercepted (see the green TTT diagram in Fig. 4). The resulting An-frequency curve is peaked at the lowest anorthite content and distributed over a great number of compositional classes (Fig. 3).

These three different crystallization paths, qualitatively summarized by the use of TTT diagrams, highlight that, under rapid cooling rates, the first nucleation event occurs at high degrees of undercooling (Kirkpatrick et al. 1983; Lasaga, 1997; Lesher et al. 1999). Under relatively low temperatures, the ion mobility is limited and Al-rich plagioclases are more favored with respect to Si-rich crystals. Kinetically-controlled conditions lead to the nucleation of metastable plagioclases significantly below the liquidus temperature. However, these crystals show compositions comparable to those of equilibrium when plagioclases crystallize near liquidus conditions.

Thermometric implications

Thermometers derived through the plagioclase-liquid exchange reaction between albite and anorthite components are based on the observation that the anorthite concentration in plagioclase increases with increasing temperature (Putirka, 2005 and references therein). Here we have tested one of these thermometers using as input data the multiple compositions of the plagioclase and the composition of the residual melt. This strategy is supported by the following considerations: (i) the composition of the residual melt is mostly controlled by the final crystal content rather than chemical gradients; (ii) the most suitable plagioclase-based thermometer has an error of temperature estimate of 36 °C; (iii) if local equilibrium is attained between the crystal rim and the coexisting melt, this equilibrium condition cannot be appreciated within the uncertainty of the thermometer; (iv) large, compositionally heterogeneous plagioclases growth by agglomeration of single crystals (iv) by using these heterogeneous compositions as input data for the thermometer, it is possible to determine the thermal path of the cooling system driving successive nucleation events. Results are reported in the Microsoft Excel spreadsheet available online as supplementary material. The chosen

activity model has been derived by new global regression analyses yielding the following thermometric equation (Putirka, 2005; 2008):

$$\frac{10^4}{T(K)} = 6.4706 + 0.3128 \ln\left(\frac{X_{An}^{pl}}{X_{CaO}^{melt}\left(X_{AlO_{1.5}}^{melt}\right)^2\left(X_{SiO_2}^{melt}\right)^2}\right) - 8.103\left(X_{SiO_2}^{melt}\right) + 4.872\left(X_{KO_{0.5}}^{melt}\right) + 1.5346\left(X_{Ab}^{pl}\right)^2 + 8.661\left(X_{SiO_2}^{melt}\right)^2 - 3.341\times10^{-2}(P(kbar)) + 0.18047\left(H_2O^{melt}\right)$$

(R^2 = 0.93 and SEE = 36 °C) (Eqn. 1)

Mineral components of Eqn. 1 are calculated as cation fractions according to $X_{An}^{pl} = X_{CaO}^{pl} / \left(X_{CaO}^{pl} + X_{NaO_{0.5}}^{pl} X_{KO_{0.5}}^{pl}\right)$ and $X_{Ab}^{pl} = X_{NaO_{0.5}}^{pl} / \left(X_{CaO}^{pl} + X_{NaO_{0.5}}^{pl} X_{KO_{0.5}}^{pl}\right)$. Fig. 7 shows that temperature estimates obtained through the thermometer significantly change from 1030 °C to 1170 °C. An important outcome from Fig. 5 is that, with increasing cooling rate, predicted temperatures monotonically approach to the plagioclase saturation temperature of 1165 °C calculated by the MELTS code (Ghiorso and Sack 1995). Crystals and melts show disequilibrium compositions over an ever-changing temperature comprised between the liquidus and final temperature of the crystal growth (Fig. 5). Consequently, the temperatures predicted by the thermometer are distributed over a wide thermal range (Fig. 5). Histograms calculated using 7 bins for each temperature interval 20 °C are plotted in Fig. 6 showing that: (i) at 25 °C/min, the thermometric estimate yields an almost constant value of 1160 °C; (ii) at 12.5 °C/min, the peak is still at 1160 °C but a few data indicate crystallization at 1040 °C; (iii) at 3 °C/min, the temperature estimates is comprised between 1160 and 1120 °C and; (iv) at both 0.5 and 0.125 °C/min, the majority of the data suggest crystallization temperatures of 1120 and 1080 °C, respectively. To shed light on the relationship between plagioclase composition and temperature estimate, we have drawn in Fig. 7 three different Ab-An plagioclase loop binary diagrams by using (i) equilibrium data calculated by the MELTS code and (ii) cooling rate data obtained at 0.125 and 25 °C/min. The bulk rock calc-alkaline composition is An_{53} and corresponds to the starting liquid plotted in Fig. 7. Under equilibrium crystallization conditions, the tie line passing through An_{53} intercepts the liquidus loop at 1165 °C yielding plagioclase composition of An_{74} (Fig. 7). As the temperature decreases to 800 °C, the residual melt composition approaches to An_{28} (Fig. 7). Conversely, at the slowest cooling rate of 0.125 °C/min, the anorthite in plagioclase decreases from An_{96} to An_{34} yielding crystallization temperatures around a thermal range from 1080 to 1030 °C (Fig. 7). The binary loop topology results to be flattened minimizing the temperature difference between liquidus and solidus to a value of 50 °C. A

similar loop shape is obtained at the fastest cooling rate of 25 °C/min (Fig. 7). However, the convex upward liquidus and the convex downward solidus are shifted toward higher temperatures (Fig. 7); as a consequence, the plagioclase crystals show a more restricted compositional variation of An_{60-96} within a temperature interval of 20 °C only. This implies that the residual melt composition (An_{50}) closely matches to that (An_{53}) of the calc-alkaline bulk rock (Fig. 7), in agreement with the lowest crystal content measured at 25 °C/min (Table 1).

Since the Ab-An binary loop diagram is based on the assumption of equilibrium partitioning between crystal and melt, any form of disequilibrium would alter the shape of the loop (Fig. 7). In fact, under dynamic crystallization conditions, chemical elements do not fractionate at the equilibrium proportion and distribution coefficients progressively depart from the equilibrium value (e.g., Mollo et al., 2011a and references therein). Moreover, our data highlight that the degree of crystallization progressively decreases with increasing cooling rate (Table 1). Therefore, increasing degrees of undercooling leads to the formation of more primitive melts coexisting with plagioclase crystals progressively enriched in anorthite (Fig. 3). In light of this disequilibrium due to cooling kinetics, plagioclase-based thermometers estimate crystallization temperatures higher than predicted at equilibrium (Fig. 6). Results from our chemical maps highlight that the disequilibrium composition of plagioclase can serve to decipher the thermal history of rapidly cooled melts. Fig. 7 shows that equilibrium plagioclase crystals grow over a temperature range of 365 °C comprised between the liquidus (1165 °C) and the final solidus (800 °C) temperature of the system. Conversely, at 0.125 and 25 °C/min, the plagioclase compositional variation records lower thermal paths of 50 and 20 °C, respectively (Fig. 7).

This has important implications for the estimate of post-eruptive solidification conditions. Lava flows and intrusive bodies from centimeters to a few meters thick are characterized by an intense heat loss, a short solidification time and a strong thermal diffusion (Ujike 1982; Pietranik et al. 2006; Chistyakova and Latypov 2009; Del Gaudio et al. 2010; Mollo et al., 2011b). Under such circumstances, plagioclase-based thermometers could provide erroneous temperature estimates of crystallization. This conclusion can also be potentially extended to magma ascent processes where rapid kinetic conditions are induced by depressurization accompanied by volatile release. As pointed out by Blundy and Cashman (2008) and Brugger and Hammer (2010), rapid decompression paths determine high degree of undercooling and plagioclase microlites do not maintain chemical equilibrium with melt and are more anorthite-rich than equilibrium plagioclase. This suggests that interpretations of magma ascent processes in nature require comparisons with dynamic rather than static (phase equilibrium) experiments (cf. Brugger and Hammer 2010). The use of microprobe mapping to obtain statistical distribution of plagioclase compositions may be important to quantify

magma thermal and pressure gradients and to discriminate between equilibrium and disequilibrium processes.

IMPLICATIONS

Microprobe investigations conducted by selection of single point analyses and by crystal core-to-rim analytical profiles do not fully represent the chemical processes driving the nucleation and growth of plagioclase, and possibly other volcanic crystals, under dynamic crystallization conditions. Due to the slow coupled CaAl–NaSi interdiffusion, the re-equilibration of crystals is inhibited and growing plagioclases record any compositional variation of the melt. Under fast cooling rate conditions, plagioclases enriched in anorthite are metastably crystallized at high degrees of undercooling due to the weaker Al-O bond than Si-O bond. Conversely, under slow cooling rate conditions, successive and repeated nucleation events cause crystallization of An-poor crystals that approach equilibrium compositions such as An_{56} for our investigated andesitic melt (Fig. 3). Using chemical mapping, we have found the presence of two discrete plagioclase populations (i.e., An-rich and An-poor) at the intermediate cooling rate of 3 °C/min. The most important outcome from this study is the occurrence of a wide spectrum of plagioclase compositions obtained from a single (superheated) homogeneous andesitic melt cooled at different rates. TTT diagrams can be used to explain the compositional variability of plagioclase as the result of successive and repeated nucleation events from a more differentiated melt (Fig. 4). Moreover, the disequilibrium composition of plagioclase can serve to decipher the thermal history of rapidly cooled melts (Fig. 7). Plagioclase-based thermometers may determine the variable thermal gradients driving the solidification path of rapidly cooled rocks and leading to the formation of An-rich crystals.

ACKNOWLEDGEMENTS

Authors are grateful to D. Dolfi for allowing us to use experimental petrology facilities at the Università degli Studi Roma Tre (Roma). This study was funded by “Fondi Ateneo of the University G. d’Annunzio” and by PRIN project “Experimental determination of the glass-forming ability (GFA), nucleation and crystallization of natural silicate melts” awarded to G. Iezzi. S. Mollo was supported by the ERC Starting grant 259256 GLASS project. The research activities of the HP-HT laboratory of the INGV were supported by the European Observing System Infrastructure Project (EPOS).

REFERENCES CITED

Baker, D.R. (2008). The fidelity of melt inclusions as records of melt composition. Contributions to Mineralogy and Petrology 157: 377–395.

Baschek, G., and Johannes, W. (1995) The estimation of NaSi-CaAl interdiffusion rates in peristerite by homogenization experiments**.** European Journal of Mineralogy, 7, 295-307.

Blundy, J., Cashman, K., and Humphreys, M. (2006) Magma heating by decompression-driven crystallization beneath andesite volcanoes. Nature, 443, 76-80.

Blundy, J., and Cashman, K. (2008) Petrologic reconstruction of magmatic system variables and processes. In K.D. Putirka and F.J. Tepley, Eds., Minerals, Inclusions and Volcanic Processes, 69, p. 179-239. Reviews in Mineralogy and Geochemistry, Mineralogical Society of America, Chantilly, Virginia.

Brugger, C.R., and Hammer, J.E. (2010) Crystallization Kinetics in Continuous Decompression Experiments: Implications for Interpreting Natural Magma Ascent Processes. Journal of Petrology, 51, 1941-1965.

Burkhard, D.J.M. (2005) Crystallization and oxidation during emplacement of lava lobes. In: Manga, M., Ventura, G (Eds.), Geological Society of America, Special Paper 396, pp. 67-80.

Chistyakova, S., and Latypov, R. (2009) On the development of internal chemical zonation in small mafic dikes. Geological Magazine, 147, 1-12.

Corrigan, G.M. (1982) The crystal morphology of plagioclase feldspar produced during isothermal supercooling and costant rate cooling experiments. Mineralogical Magazine 46, 433-439.

Couch, S., Sparks, R.S.J., Carroll, M.R.(2001) Mineral disequilibrium in lavas explained by convective self-mixing in open magma chambers. Nature 411, 1037-1039.

Couch, S., Sparks, R. S. J. & Carroll, M. R. (2003) The kinetics of degassing-induced crystallization at Soufriere Hills volcano, Montserrat. Journal of Petrology 44, 1477-1502.

Deer, W.A., Howie, R.A., and Zussman, J. (2001) Framework silicates: feldspars, 972 p. The Geological Society, London.

Del Gaudio, P., Mollo, S.,Ventura, G., Iezzi, G., Taddeucci, I., and Cavallo, A. (2010) Cooling rate-induced differentiation in anhydrous and hydrous basalts at 500 MPa: Implications for the storage and transport of magmas in dikes. Chemical Geology, 270, 164-178.

Dingwell, D.B. (1995) Relaxation in silicate melts: some applications in petrology. In: J. F. Stebbins, D.B. Dingwell and P.W. McMillan, Eds., Structure and Dynamics of silicate melts, 32, p. 21-66. Reviews in Mineralogy and Geochemistry, Mineralogical Society of America, Chantilly, Virginia.

Dingwell, D.B. (2006) Transport properties of magmas: diffusion and rheology. Elements 2, 281-286.

Dolfi, D., De Rita, D., Cimarelli, C., Mollo, S., Soligo, M., and Fabbri, M. (2007) Dome growth rates, eruption frequency and assessment of volcanic hazard: Insights from new U/Th dating of the Panarea and Basiluzzo dome lavas and pyroclastics, Aeolian Islands, Italy. Quaternary International, 162-163, 182-194.

Dunbar, N.W., Jacobs, G.K., and Naney, M.T. (1995) Crystallization processes in an artificial magma: variations in crystal shape, growth rate and composition with melt cooling history. Contribution to Mineralogy and Petrology, 120, 412-425.

Fokin, V.M., Zanotto, E.D., and Schmelzer, J.W.P. (2003) Homogeneous nucleation versus glass transition temperature of silicate glasses. Journal of Non-Crystalline Solids, 321, 52-65.

Frey, H.M., Lange, R.A. (2011) Phenocryst complexity in andesites and dacites from the Tequila volcanic field, Mexico: resolving the effects of degassing vs. magma mixing. Contribution to Mineralogy and Petrology, 162, 415-445.

Ghiorso, M.S., and Sack, R.O. (1995) Chemical mass-transfer in magmatic processes 4. A revised and internally consistent thermodynamic model for the interpolation and extrapolation of liquid-solid equilbria in magmatic systems at elevated temperatures and pressures. Contribution to Mineralogy and Petrology, 119, 197-212.

Grove, T.L., Baker, M.B., and Kinzler, R.J. (1984) Coupled CaAl-NaSi diffusion in plagioclase feldspar: Experiments and applications to cooling rate speedometry. Geochimica et Cosmochimica Acta, 48, 2113-2121.

Hammer, J.E. (2006) Influence of fO_2 and cooling rate on the kinetics and energetics of Fe-rich basalt crystallization. Earth and Planetary Science Letters, 248, 618-637.

Hammer, J.E. (2008) Experimental studies of the kinetics and energetics of magma crystallization. In K.D. Putirka and F.J. Tepley, Eds., Minerals, Inclusions and Volcanic Processes, 69, p. 9-59. Reviews in Mineralogy and Geochemistry, Mineralogical Society of America, Chantilly, Virginia.

Higgins, M.D. (2011) Textural coarsening in igneous rocks. International Geology Review, 53, 354-376.

Iezzi, G., Mollo, S., Ventura, G., Cavallo, A., and Romano, C. (2008) Experimental solidification of anhydrous latitic and trachytic melts at different cooling rates: the role of nucleation kinetics. Chemical Geology, 253, 91-101.

Iezzi, G., Mollo, S., Ventura, G. (2009) Solidification behaviour of natural silicate melts and volcanological implications. In N. Lewis and A. Moretti, Eds., Volcanoes: Formation, Eruptions and Modelling, p 127-151 Nova publishers, New York.

Iezzi, G., Mollo, S., Torresi, G., Ventura, G., Cavallo, A., and Scarlato, P. (2011) Experimental solidification of an andesitic melt by cooling. Chemical Geology, 283, 261-273.

Kirkpatrick, R.J. (1983) Theory of nucleation in silicate melts. American Mineralogists, 68, 66-77.

Kirkpatrick, R.J., Reck, B.H., Pelly, I.Z., and Kuo, L.-C. (1983) Programmed cooling experiments in the system MgO-SiO_2: kinetics of a peritectic reaction. American Mineralogist, 68, 1095-1101.

Lanzafame, G., Mollo, S., Iezzi, G., Ferlito, C., and Ventura, G. (2013) Unraveling the solidification path of a pahoehoe "cicirara" lava from Mount Etna volcano. Bulletin of Volcanology, 75, DOI 10.1007/s00445-013-0703-8.

Lasaga, A.C. (1997) Kinetic Theory in the Earth Sciences, p. 811. Princeton University Press, New York.

Lesher, C.E., Cashman, K.V., and Mayfield, J.D. (1999) Kinetic controls on crystallization of Tertiary North Atlantic basalt and implications for the emplacement and cooling history of lava at Site 989, Southeast Greenland rifted margin. In H.C. Larsen, R.A. Duncan, J.F. Allan, and K. Brooks, Eds., 163, p. 1-14. Proceedings of the Ocean Drilling Program, Scientific Results, College Station, TX (Ocean Drilling Program), doi:10.2973/odp.proc.sr.163.115.1999.

Liu, M., and Yund, R.A. (1992) NaSi-CaAl interdiffusion in plagioclase**.** American Mineralogist 77, 275-283.

Lofgren, G.E. (1974) An experimental study of plagioclase morphology: Isothermal crystallization. American Journal of Science 264, 243-273.

Lofgren, G. (1980). Experimental studies on the dynamic crystallization of silicate melts. In R.B. Hargraves, Ed., Physics of Magmatic Processes, p. 487. Princeton University Press, Princeton, New Jersey.

Loomis, T.P. (1981) An investigation of disequilibrium growth processes of plagioclase in the system anorthite-albite-water by methods of numerical simulation. Contributions to Mineralogy and Petrology, 81, 219-229.

Marsh, B.D. (1988) Crystal capture, sorting, and retention in convecting magma. Bulletin of the Geological Society of America, 100, 1720-1737.

Mattioli, M., Renzulli, A., Menna, M., and Holm, P.M. (2006) Rapid ascent and contamination of magmas through the thick crust of the CVZ (Andes, Ollague region): Evidence

573 from a nearly aphyric high-K andesite with skeletal olivines. Journal of Volcanology and
574 Geothermal Research, 158, 87-105.
575 Mollo, S., Del Gaudio, P., Ventura, G., Iezzi, G., Scarlato, P. (2010) Dependence of
576 clinopyroxene composition on cooling rate in basaltic magmas: Implications for thermobarometry.
577 Lithos, 118, 302-312, doi:10.1016/j.lithos.2010.05.006.
578 Mollo, S., Putirka, K.D., Iezzi, G., Del Gaudio, P., and Scarlato, P. (2011a) Plagioclase-melt
579 (dis)equilibrium due to cooling dynamics: implications for thermometry, barometry and hygrometry,
580 Lithos, 125, 221-235, doi:10.1016/j.lithos.2011.02.008.
581 Mollo, S., Lanzafame, G., Masotta, M., Iezzi, G., Ferlito, C., and Scarlato P. (2011b) Cooling
582 history of a dike as revealed by mineral chemistry: A case study from Mt. Etna volcano, Chemical
583 Geology, 283, 261-273, doi:10.1016/j.chemgeo.2011.06.016.
584 Mollo, S., Misiti, V., Scarlato, P., and Soligo, M., (2012a) The role of cooling rate in the
585 origin of high temperature phases at the chilled margin of magmatic intrusions, Chemical Geology,
586 322-323, 28-46, doi:10.1016/j.chemgeo.2012.05.029.
587 Mollo, S., Iezzi, G., Ventura, G., Cavallo, A., and Scarlato, P. (2012b) Heterogeneous
588 nucleation mechanisms and formation of metastable phase assemblages induced by different
589 crystalline seeds in a rapidly cooled andesitic melt, Journal of Non-Crystalline Solids, 358, 1624-
590 1628.
591 Morse, S.A. (1984) Cation diffusion in plagioclase feldspar. Science, 225, 504-505.
592 Moynihan, C.T. (1995) Structural Relaxation and the Glass Transition. In: J.F. Stebbins,
593 D.B. Dingwell, and P.W. McMillan, Eds., Structure and Dynamics of silicate melts, 32, p. 1-20.
594 Reviews in Mineralogy and Geochemistry, Mineralogical Society of America, Chantilly, Virginia.
595 Muir, D. D., Blundy, J. D., and Rust, A. C. (2012) Multiphase petrography of volcanic
596 rocks using element maps: a method applied to Mount St. Helens, 1980–2005. Bulletin of
597 Volcanology, 74,1101-1120.
598 Mysen, B.O., and Richet, P. (2005) Silicate glasses and melts: properties and structure, p.
599 544. Developments in Geochemistry 10, Elsevier, Amsterdam.
600 Neri, A. (1998) A local heat transfer analysis of lava cooling in the atmosphere: application
601 to thermal diffusion-dominated lava flows. Journal of Volcanology and Geothermal Research, 81,
602 215-243.
603 Pietranik, A., Koepkeb, J., and Puziewicza, J. (2006) Crystallization and resorption in
604 plutonic plagioclase: Implications on the evolution of granodiorite magma (Gęsiniec granodiorite,
605 Strzelin Crystalline Massif, SW Poland). Lithos, 86, 260-280.

606 Pieczka, A., Buniak, A., Majka, J., and Harryson H. (2011) Si-deficient foitite with [4]Al and
607 [4]B from the 'Ługi-1' borehole, southwestern Poland. Journal of Geosciences, 56, 389-398.
608 Pownceby, M.I., and McCrae C.M. (2007a) Electron microbeam analysis techniques used for
609 the characterization of industrial minerals. In: Advances in the characterization of industrial
610 minerals, G.E. Christidis, Ed., 9, p. 227-286. EMU Notes in Mineralogy, The Mineralogical Society
611 of Great Britain and Ireland, London.
612 Pownceby, M.I., McCrae, C.M., and Wilson, N.C. (2007b) Mineral characterization by
613 EPMA mapping. Minerals Engineering, 20, 444-451.
614 Pret, D., Sammartino, S., Beaufort, D., Meunier, A., Fialin, M., and Michot, L.J. (2010a) A
615 new method for quantitative petrography based on image processing of chemical element maps: Part
616 I. Mineral mapping applied to compacted bentonites. American Mineralogist, 95, 1379-1388.
617 Pret, D., Sammartino, S., Beaufort, D., Fialin, M., Sardini, P., Cosenza, P., and Meunier, A.
618 (2010b). A new method for quantitative petrography based on image processing of chemical element
619 maps: Part II. Semi-quantitative porosity maps superimposed on mineral maps. American
620 Mineralogist, 95, 1389-1398.
621 Putirka, K.D. (2005) Igneous thermometers and barometers based on plagioclase+liquid
622 equilibria: test of some existing models and new calibrations. American Mineralogist, 90, 336–346.
623 Putirka, K.D. (2008) Thermometers and barometers for volcanic systems. In K.D. Putirka
624 and F.J. Tepley, Eds., Minerals, Inclusions and Volcanic Processes, 69, p. 61–120. Reviews in
625 Mineralogy and Geochemistry, Mineralogical Society of America, Chantilly, Virginia.
626 Roskosz, M., Toplis, M.J., and Richet, P. (2006a) Kinetic vs. thermodynamic control of
627 nucleation and growth in molten silicates. Journal of Non-Crystal Solids 352, 180-184.
628 Roskosz, M., Toplis, M.J., and Richet, P. (2006b) Crystallization of highly supercooled
629 silicate melts. Advanced Engineering Materials, 8, 1224-1228.
630 Schiavi, F., Walte, N., and Keppler, H. (2009) First in-situ observation of the crystallization
631 processes in a basaltic–andesitic melt with the moissanite cell. Geology 37, 963-966.
632 Shea, T., and Hammer, J.E. (2013) Kinetics of cooling- and decompression-induced
633 crystallization in hydrous mafic-intermediate magmas. Journal of Volcanology and Geothermal
634 research, 260, 127-145.
635 Singer, B.S., Dungan, M.A., and Layne, G.D. (1995) Textures and Sr, Ba, Mg, Fe, K and Ti
636 compositional profiles in volcanic plagioclase: clues to the dynamics of calcalkaline magma
637 chambers. American Mineralogist 80, 776-798.
638 Smith, J.Y., and Brown, W.L. (1988) Feldspar minerals vol. I: Crystal structures, physical,
639 chemical, and microtextural properties, 2nd edition, p. 828. Springer, Berlin.

Tamura, Y., Yuhara, M., Ishii, T., Irino, N., and Shukuno, H. (2003) Andesites and dacites from Daisen Volcano, Japan: Partial-to-total remelting of an andesite magma body. Journal of Petrology, 12, 2243-2260.

Teng, H.H. (2013) How ions and molecules organize to form crystals. Elements, 9, 189-194.

Uhlmann, D.R., Onorato, P.I.K., and Scherer, G.W. (1979) A simplified model for glass formation. Lunar and Planetary Science Conference, 1, 375-381.

Ujike, O. (1982) Microprobe mineralogy of plagioclase, clinopyroxene and amphibole as records of cooling rate in the Shirotori-Hiketa dike swarm, northeastern Shikoku, Japan. Lithos 15, 281-293.

Vetere, F., Iezzi, G., Behrens, H., Cavallo, A., Misiti, V., Dietrich, M., Knipping, J., Ventura, G., and Mollo, S. (2013) Intrinsic solidification behaviour of basaltic to rhyolitic melts: A cooling rate experimental study. Chemical Geology, 354, 233-242.

Webb, S.L. (2005) Silicate melts at extreme conditions In Mineral Behaviours at Extreme Conditions, R. Miletich, Ed., 7, 64-95. EMU Notes In Mineralogy, he Mineralogical Society of Great Britain and Ireland, London.

Welsch, B., Faure, F., Famin, V., Baronnet, A., and Bachèlery, P. (2013) Dendritic crystallization: a single process for all the textures of olivine in basalts?. Journal of Petrology, 54, 539-574.

Xu, Z., and Zhang, Y. (2002) Quench rates in water, air and liquid nitrogen and inference of temperature in volcanic eruption columns. Earth and Planetary Science Letters, 200, 315-330.

Zhang, Y. (2008). Geochemical kinetics, p. 656. Princeton University Press, New York.

Table 1. Analytical conditions of chemical maps.

cooling rate (°C/min)	area (μm^2)	sampling distance (μm)	number of points	crystal content (vol.%)
25	61×10^3	2	1.656	10
12.5	338×10^3	2	824	20
3	143×10^3	2	1.320	28
0.5	637×10^3	4	4.110	78
0.125	5.413×10^3	4	4.365	80

Footnote: the crystal content of each run products measured by Iezzi et al. (2011) is also reported in table. The number of point analyses refer to the plagioclase compositions matching with those reproduced by the ternary feldspar system (i.e., 43.2< SiO_2 <68.7, 18.3< Al_2O_3 <36.7, 0< CaO <20.2, 0< Na_2O <11.8 and 0< K_2O <16.9 all in wt.%). These compositions were also selected in order to have the sum of oxide components comprised between 99 and 101 wt.%.

Figure captions

Figure 1. Microprobe maps of SiO_2, Al_2O_3 and CaO (a), and Na_2O, K_2O and An (b) measured in each experimental run-product. Large and tiny plagioclase crystals are indicated in the An maps.

Figure 2. Chemical variations of Al_2O_3, CaO, Na_2O and K_2O as a function of SiO_2. Five different diagrams are presented in figure for each cooling rate run.

Figure 3. Distribution histograms and An-frequency curves of plagioclase. Histograms were calculated using 20 bins for each 5 mol.% of An. The composition of plagioclase in equilibrium with the andesitic melt (i.e., An_{57}) is also depicted using the dashed line. This composition comes from plagioclases equilibrated at the final quenching temperature of 800 °C. The anorthite content values for the melt composition are also reported.

Figure 4. TTT diagrams relating nucleation rate (I), temperature (T), and induction time (τ). T_m is the melting or liquidus temperature, whereas T_g is the glass transition temperature (at 10^{12} Pa s). Three different cooling rate conditions of 25, 3 and 0.125 °C/min are also reported in figure. As the cooling rate increases, plagioclase are progressively enriched in anorthite due to successive nucleation events.

Figure 5. As the cooling rate is increased, each temperature estimated by using plagioclase-based thermometer approach to the plagioclase saturation temperature of 1165 °C.

Figure 6. Histograms calculated using 7 bins for each temperature interval 20 °C. Generally, the temperature estimate progressively increases with increasing cooling rate. However, at 3 °C/min, the temperature estimates is comprised between 1160 and 1120 °C resembling the different crystallization events that produce An-rich plagioclases at the early stage of cooling and An-poor crystals from the more differentiated melt.

Figure 7. Three different Ab-An plagioclase loop binary diagrams are obtained by using (i) equilibrium data calculated by the MELTS code and (ii) cooling rate data obtained at 0.125 and 25 °C/min. The bulk rock calc-alkaline composition is An_{53} and represents the starting liquid plotted in figure.

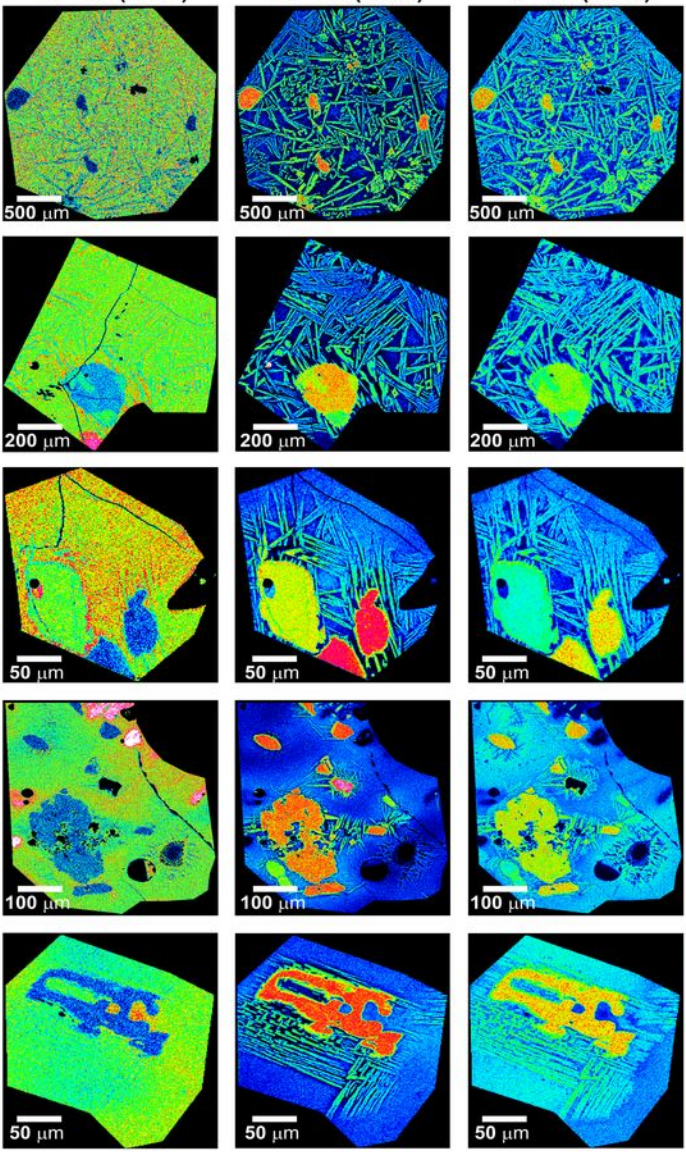
SiO2
40 - 80 (wt.%)
Al2O3
10 - 45 (wt.%)
CaO
0 - 30 (wt.%)
0.125 °C/min
0.5 °C/min
3 °C/min
12.5 °C/min
25 °C/min
500 µm
200 µm
50 µm
100 µm

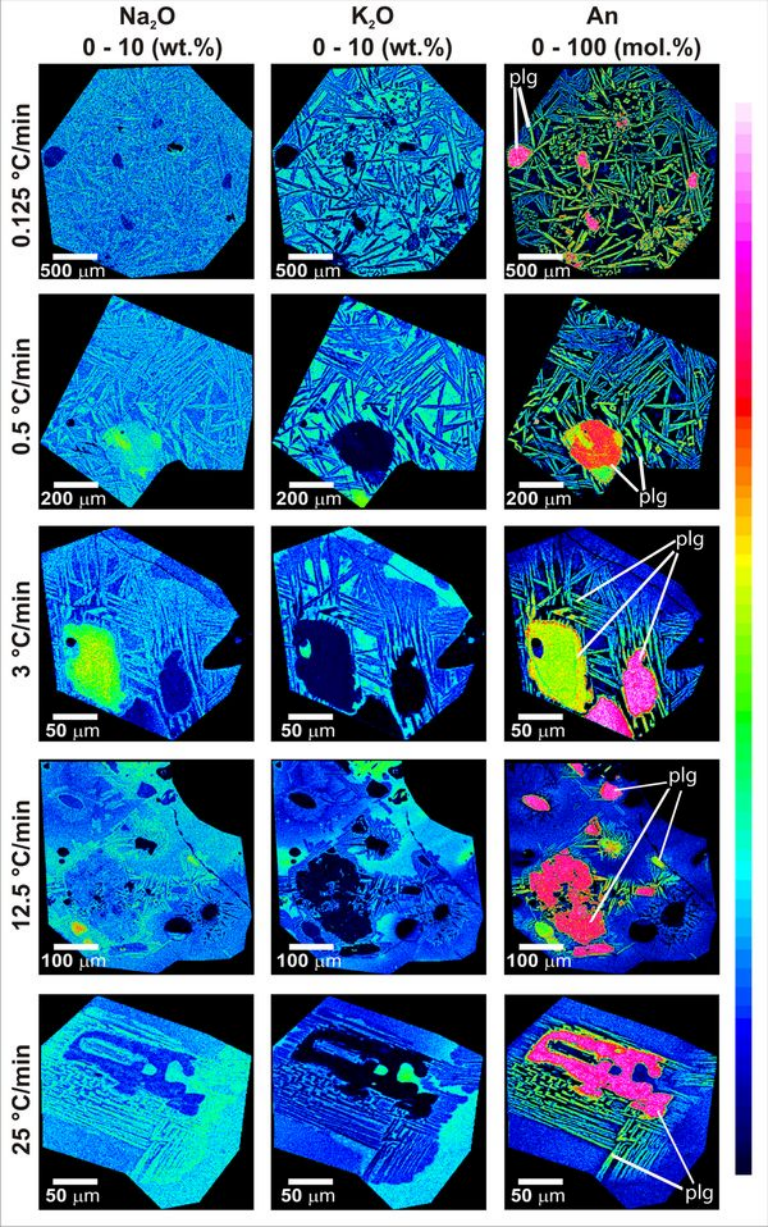
Na2O
0 - 10 (wt.%)
K2O
0 - 10 (wt.%)
An
0 - 100 (mol.%)
0.125 °C/min
0.5 °C/min
3 °C/min
12.5 °C/min
25 °C/min
500 µm
200 µm
50 µm
100 µm
plg

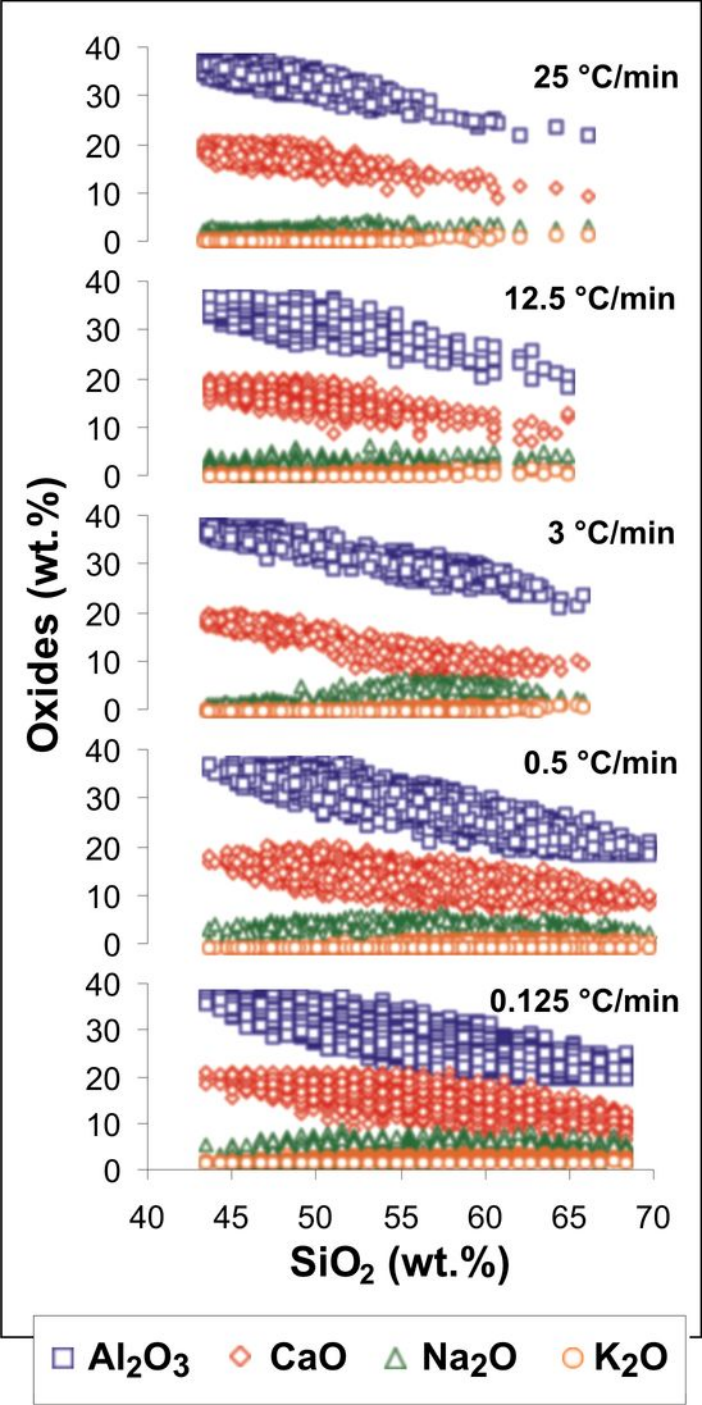
25 °C/min
12.5 °C/min
3 °C/min
0.5 °C/min
0.125 °C/min
Oxides (wt.%)
SiO2 (wt.%)
Al2O3
CaO
Na2O
K2O

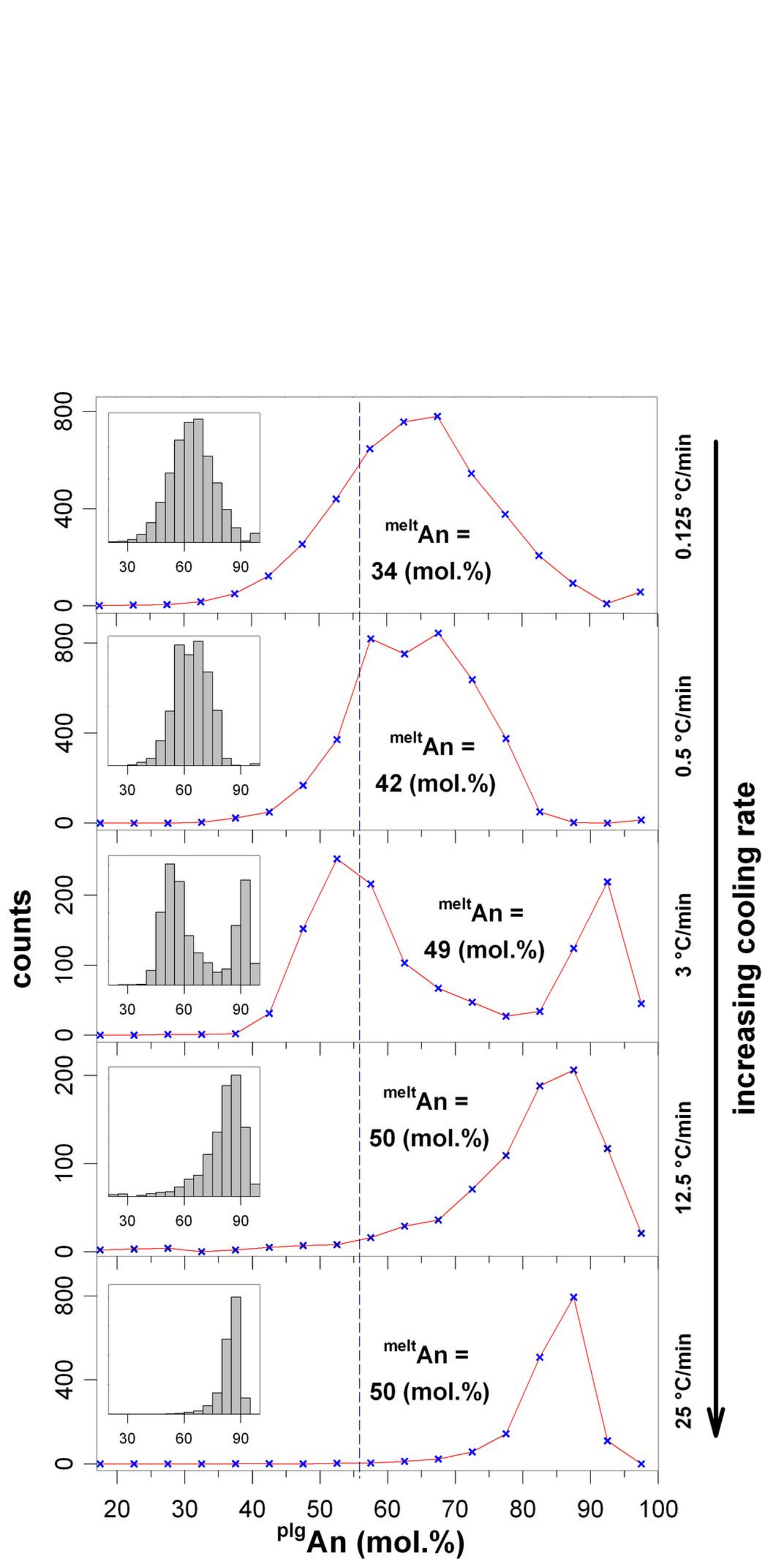
counts
0
400
800
0
100
200
0
100
200
0
400
800
30
60
90
^{melt}An =
34 (mol.%)
^{melt}An =
42 (mol.%)
^{melt}An =
49 (mol.%)
^{melt}An =
50 (mol.%)
^{melt}An =
50 (mol.%)
0.125 °C/min
0.5 °C/min
3 °C/min
12.5 °C/min
25 °C/min
increasing cooling rate
20
30
40
50
60
70
80
90
100
^{plg}An (mol.%)

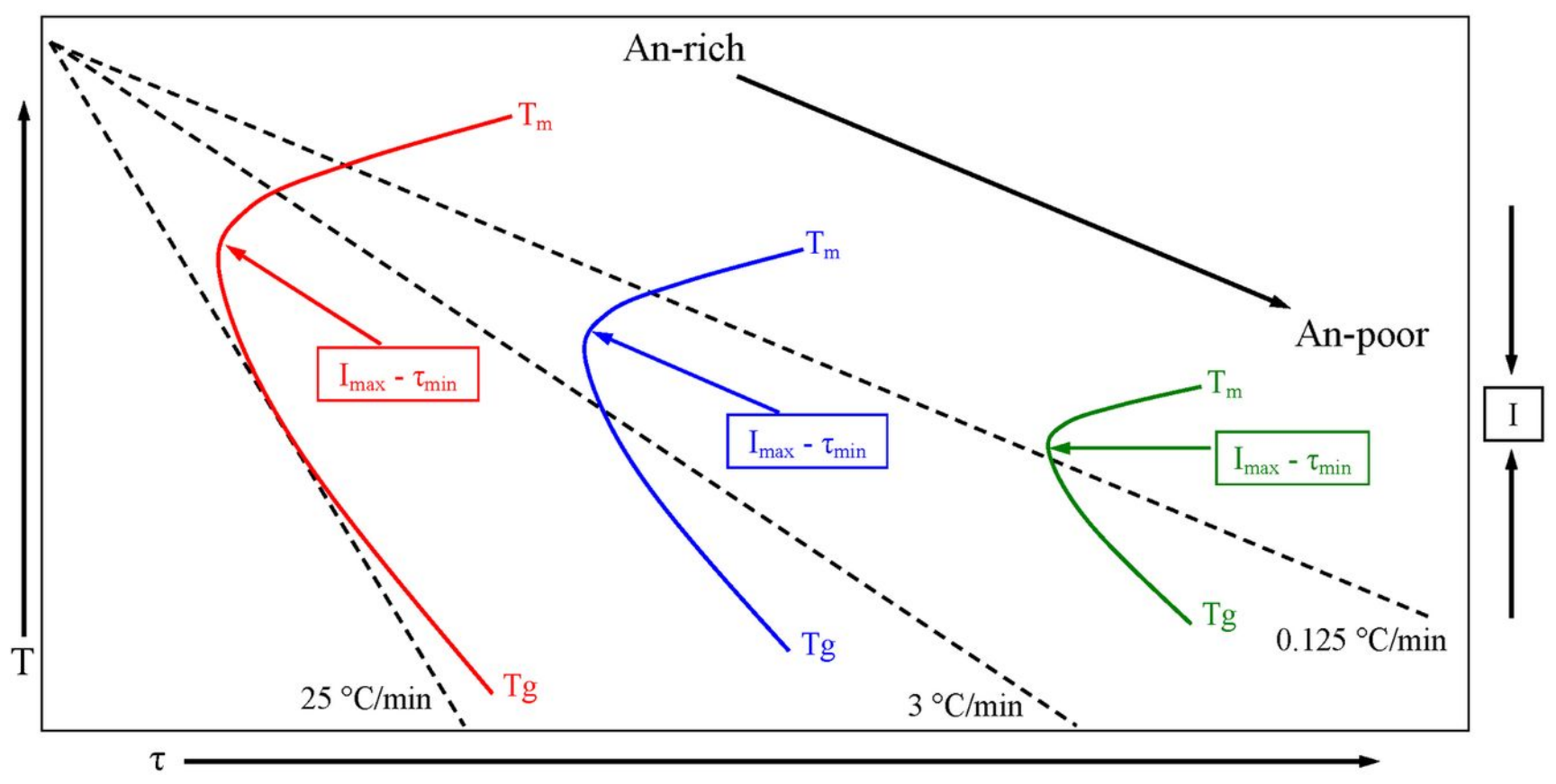
An-rich
An-poor
T_m
T_m
T_m
I_{max} - τ_{min}
I_{max} - τ_{min}
I_{max} - τ_{min}
Tg
Tg
Tg
25 °C/min
3 °C/min
0.125 °C/min
T
τ
I

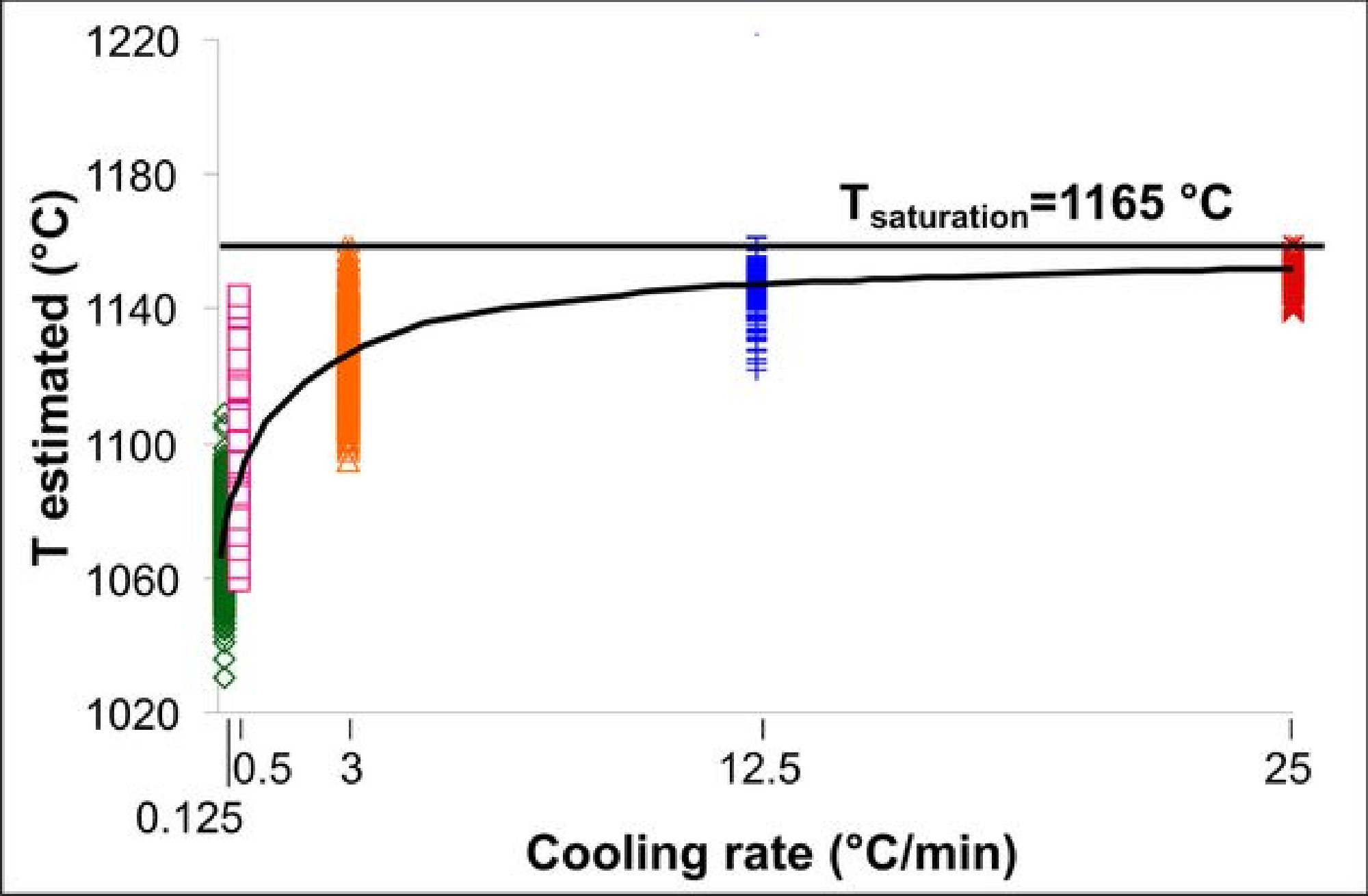
1220
1180
1140
1100
1060
1020
T estimated (°C)
T saturation=1165 °C
0.125
0.5
3
12.5
25
Cooling rate (°C/min)

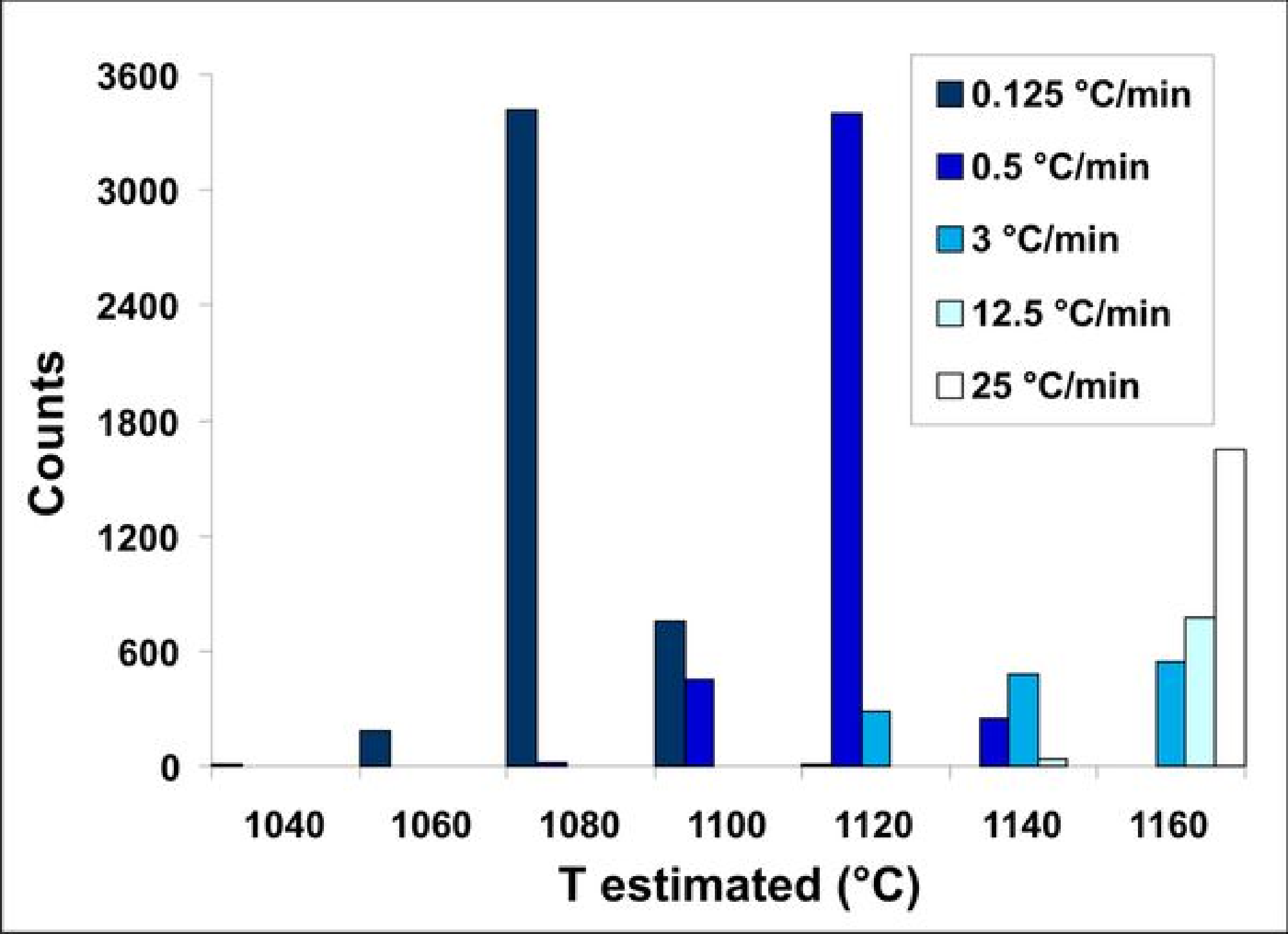
3600
3000
2400
1800
1200
600
0
Counts
0.125 °C/min
0.5 °C/min
3 °C/min
12.5 °C/min
25 °C/min
1040
1060
1080
1100
1120
1140
1160
T estimated (°C)

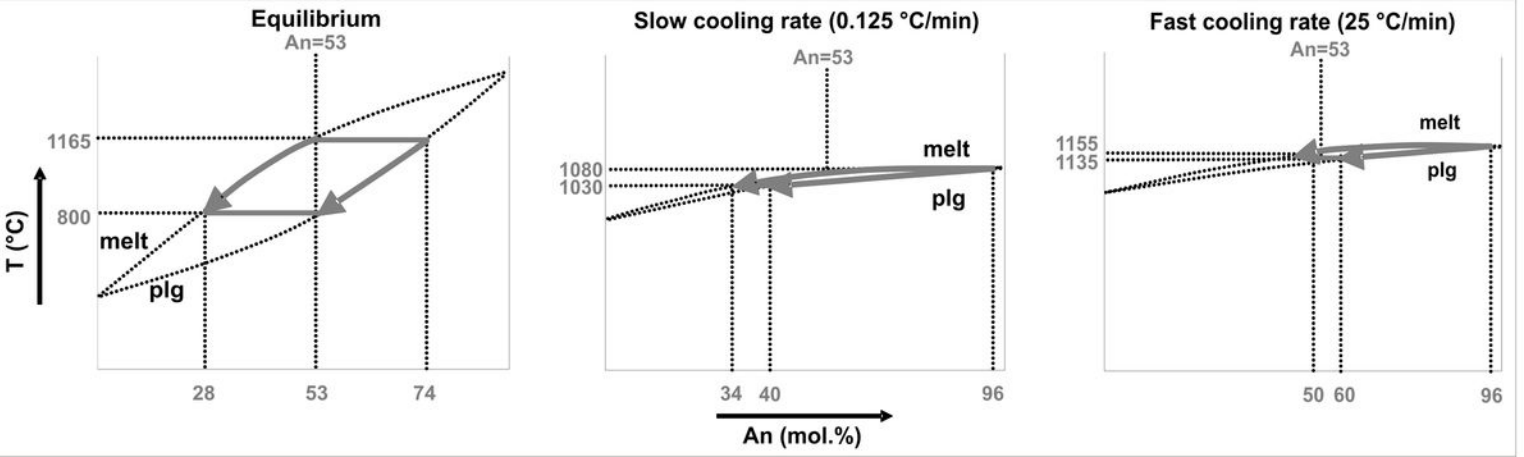
Equilibrium
An=53
1165
800
T (°C)
melt
plg
28
53
74
Slow cooling rate (0.125 °C/min)
An=53
1080
1030
melt
plg
34
40
96
Fast cooling rate (25 °C/min)
An=53
1155
1135
melt
plg
50
60
96
An (mol.%)